Impact of Wall Heat Losses in Large-Eddy Simulations of Methane Oxy-Flames Stabilized on a Swirled Co-Axial Injector.

Illuminati Paolo, Ronan Vicquelin

Impact of Wall Heat Losses in Large-Eddy Simulations of Methane Oxy-Flames Stabilized on a Swirled Co-Axial Injector.

Paolo Illuminati, Ronan Vicquelin

Université Paris-Saclay, CNRS, CentraleSupélec, Laboratoire EM2C, Gif-sur-Yvette, France

Abstract

The transition to cleaner energy sources has generated significant interest in oxy-combustion as an effective method to enable Carbon Capture and Storage (CCS), reducing CO_2 emissions while maintaining operational efficiency. Despite the widespread availability and high energy density of natural gas, its residual use needs to be combined with CCS to achieve carbon neutrality. In oxy-combustion, natural gas (primarily methane) is burned with pure oxygen or oxygen-enriched air, producing exhaust gases with high CO_2 concentrations that are easier to separate and capture. However, the combustion process is highly complex, driven by intricate interactions between heat release, fluid flow dynamics, and heat transfer, particularly radiative effects. Accurate modelling is therefore essential for understanding and optimizing oxy-combustion flame behavior.

This study examines two oxygen-enriched methane flames from the Degeneve et al. dataset [1], characterized by distinct swirl intensities. Flame A0 is an attached flame with no swirl in the fuel channel but a fixed swirl in the oxidizer, while flame A1, featuring an M-shaped configuration, includes swirl in both the methane and oxidizer channels.

Large Eddy Simulation (LES), combined with tabulated chemistry approaches, is used to model oxy-combustion. The non-premixed Flamelet Progress Variable (FPV) model is applied under adiabatic wall conditions. Since wall heat losses significantly affect heat transfer within the combustor and can influence flame shape, non-adiabatic FPV variants are developed and integrated into the LES framework with prescribed wall temperatures. Numerical results for different swirl configurations are compared with experimental data in terms of flame shape and flow velocity.

This work serves as a foundational step toward incorporating conjugate heat transfer and thermal radiation into a multiphysics framework for accurately predicting heat transfer in oxy-flames.

Keywords: Large-Eddy Simulation; Oxy-Combustion; Heat Loss

1. Introduction

Oxy-combustion, particularly the combustion of methane with carbon dioxide-diluted oxygen, is a promising technology for reducing pollutant formation, especially nitrogen oxides (NO_x). Additionally, it plays a crucial role in Carbon Capture and Storage (CCS) by minimizing CO_2 emissions [2]. The deliberate removal of nitrogen from the reactant mixture significantly reduces thermal NO_x formation, as described in [3]. However, this nitrogen removal introduces trade-offs: the higher oxygen concentration increases fuel reactivity and elevates flame temperatures. These effects influence combustion stability and can lead to higher localized temperatures, affecting reaction rates and emission characteristics [4].

Furthermore, when nitrogen is replaced with carbon dioxide via flue gas recirculation, the radiative properties of CO_2 become significant. Radiative heat transfer alters the local flame structure and chemical kinetics, making it essential for numerical models to account for these effects to accurately capture the flame's thermo-chemical state [4].

For safety reasons, premixed oxy-combustion systems are generally avoided, as oxygen-enriched mixtures are more prone to flashback due to their high reaction rates. Consequently, industrial applications typically favor non-premixed injector designs. Detailed experimental and numerical studies are required to understand the complex flame dynamics and stability characteristics of oxy-combustion systems. For instance, the work by Degeneve et al. [1] has shown that varying swirl intensities in oxygen-enriched flames can fundamentally alter flame stabilization modes, transitioning from attached flames to lifted or M-shaped configurations.

At the EM2C laboratory, the OxyTec burner was specifically designed to enable parametric studies of non-premixed oxy-combustion under atmospheric conditions. This burner has been used to systematically investigate oxygen-enriched methane flames, revealing how operating parameters such as the fuel swirl number S_1 influence flame morphology. In particular, flames A0 and A1 serve as benchmark cases, illustrating the transition from an attached flame to an M-shaped structure as swirl intensity increases [1].

The present work focuses on the numerical modelling of these oxy-flames. First, cold flow injection is analyzed using Large Eddy Simulation (LES) to validate the solver's ability to capture turbulent swirling flows with detailed chemistry and transport properties. For this purpose, the YALES2 CFD solver is employed [5], known for its high-fidelity simulations of complex turbulent flows. Next, the Flamelet Progress Variable (FPV) model is introduced for oxy-combustion applications. Counterflow flame simulations are used to generate a flamelet library that overs the flame space of the S-Curve, including the stable and unstable branches as well as a quenched state. The FPV flamelet table is assembled through the AGATH flame solver refAGATH.

The classical FPV framework has been extended to incorporate nonadiabatic effects. For example, Kishimoto et al. [6] introduced enthalpy defect variables to account for radiative heat losses, thereby improving the model's applicability in regimes with significant heat dissipation. Unlike other approaches that rely on automated optimization of the progress variable definition, as in [7], the present work adopts a typical definition based on key reaction products of oxy-combustion. This ensures a consistent representation of the flame structure while preserving the non-monotonicity property of the transported variables.

However, preliminary results from adiabatic simulations of Flame A0 reveal the limitations of an Adiabatic FPV model in capturing correct behaviour of post-flame burnt gases, with a continuous OH production in the burnt gas region. These findings highlight the necessity of incorporating heat losses effects to achieve a more accurate description of flame behaviour. Building upon this, the present work aims at the development of a Radiative FPV model capable of accounting for enthalpy losses across the full range of OxyTec operating conditions. By integrating a controllable radiative sink term, it is possible to artificially impose an enthalpy loss, recovering the non-adiabatic behaviour of the real flame.

2. Numerical Methods

This study utilizes the YALES2 CFD solver to numerically investigate turbulent flows, relying on the resolution of the Large Eddy Simulation (LES) under a low-Mach, variable-density formulation.

Different modelling strategies are adopted depending on the presence or absence of chemical reactions. For non-reacting flows, a detailed chemistry approach is used, incorporating a reduced kinetic mechanism that limits transported species to methane (CH_4), oxygen (O_2), and nitrogen (N_2), while accounting for detailed transport properties. In contrast, the complexity of methane combustion necessitates a tabulated chemistry approach for reacting flows, reducing the number of transported variables to passive scalars such as the Mixture Fraction (Z), its variance (Z'), and a progress variable (Y_C). When required, the enthalpy H can also be transported as a passive scalar.

The SIGMA Subgrid-Scale (SGS) turbulence model is utilized to capture unresolved scales, leveraging molecular viscosity from the kinetic mechanism in non-reacting cases and tabulated values in reacting cases. Both detailed and tabulated chemistry models utilize a mixture-averaged approach for species transport. Spatial integration is performed using a fourth-order Finite Volume (FV) scheme, ensuring high accuracy on structured meshes. However, accuracy reduces to third order in distorted regions and second order near boundaries, unless polynomial reconstruction techniques are applied. These limitations arise due to the node-centered formulation of the scheme [8].Temporal discretization follows the same order as spatial integration, as recommended in [9].

Specifically, the TFV4A (also referred to as TRK4) scheme is employed in the present study to ensure consistency in time advancement. Pressure-velocity coupling is handled using a projection method, necessitating the resolution of a Poisson equation for pressure. YALES2 includes a built-in Deflated Preconditioned Conjugate Gradient (DPCG) solver, which efficiently solves for the pressure field using a predictor-corrector approach [10].

3. Non-reacting flows

The non-reacting configurations investigated in this study aim to reproduce the experimental results presented in [1]. A total of 60 cold flow cases have been experimentally analyzed under varying swirl conditions. Among these, three configurations have been selected for detailed numerical study, as they closely resemble the flow conditions of interest in the reacting cases, specifically Flames A0 and A1.

3.1. Burner Geometry and Configurations

The OxyTec burner, developed at the EM2C laboratory, serves as platform for both the experimental and numerical studies. This device is designed to stabilize swirled, pressurized flames at atmospheric operating conditions. A schematic of the setup is provided in Fig. 1.

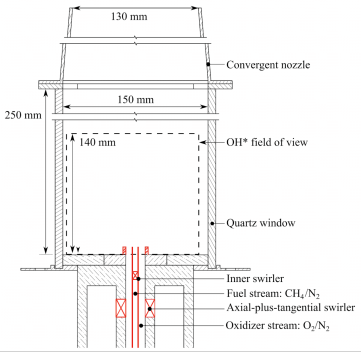

Fig. 1: Schematic of the experimental rig for the OxyTec burner. The injection swirlers are highlighted in red, and the observation windows for diagnostics are indicated.

The combustion chamber consists of a square cross-section with quartz optical windows, enabling optical access for experimental diagnostics. A converging outlet facilitates pressurized operation, while a coaxial injector supports non-premixed combustion. The inner injector, with a diameter of $d_1 = 6$ mm, delivers methane to the chamber and can impart swirl to the flow via a metallic insert, allowing for different swirl intensities. The oxidizer stream is supplied through an annular injector, with an inner diameter of 14 mm and an outer diameter of $d_2 = 20$ mm. The swirl intensity in the oxidizer stream is regulated by adjusting the volumetric flow ratio between the axial and tangential injection channels. By controlling the mass flow rates, different swirl numbers can be imposed.

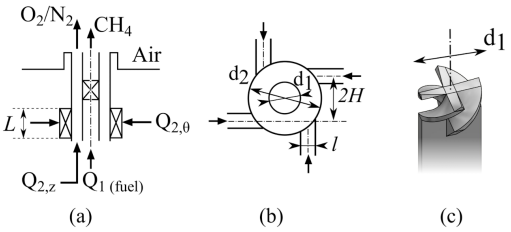

Fig. 2: Swirler schematics: (a) full system, (b) oxidizer injection, and (c) fuel injection.

In this configuration, seven interchangeable metallic inserts are available, providing trailing edge angles of $\theta_1 = 0^\circ, \pm 30^\circ, \pm 50^\circ, \pm 60^\circ$, allowing for both co-rotating and counter-rotating swirl configurations. Although the surface roughness is not optimal, the swirler is recessed within the injection channel, minimizing its impact on the flow. Experimental tests confirm that variations in surface roughness do not significantly alter the flow characteristics.

The geometrical swirl number for the methane injector is given by:

$$S_1 = \frac{1}{2}\tan(\theta) \tag{1}$$

For the oxidizer stream, swirl is introduced through four tangential injection channels, which dictate the rotational direction of the flow. The swirl number S_2 is determined by the ratio of tangential to axial flow rates and is expressed as:

$$S_2 = \frac{\pi}{4}\frac{Hd_2}{NlL}\frac{1-(d_1/d_2)^4}{1+Q_{2,z}/Q_{2,\theta}} \tag{2}$$

where: $H = 9$ mm is the radial offset between the tangential injection channels and the burner axis, $l = 3$ mm is the channel width, $L = 10$ mm is the channel height, $N = 4$ represents the number of tangential injection channels. Finally, a key parameter to fix the mass flow rates is the momentum flux ratio:

$$J = \frac{\rho_{ox} u_{z,ox}^2}{\rho_{fu} u_{z,fu}^2} \tag{3}$$

The bulk velocities of the fuel and oxidizer are 15.0 $\frac{m}{s}$ and 10.2 $\frac{m}{s}$, respectively. Based on the total length of the combustion chamber, a characteristic time is defined as in Eq. 4, for the OxyTec burner, $\tau \approx 0.037$ s. To ensure statistically meaningful data collection, the simulation was run for an initial transient period of 5τ, followed by an additional 5τ for final statistical averaging, resulting in a total simulation time of 10τ.

$$\tau = \frac{max(U_{bulk})}{L_{chamber}} \tag{4}$$

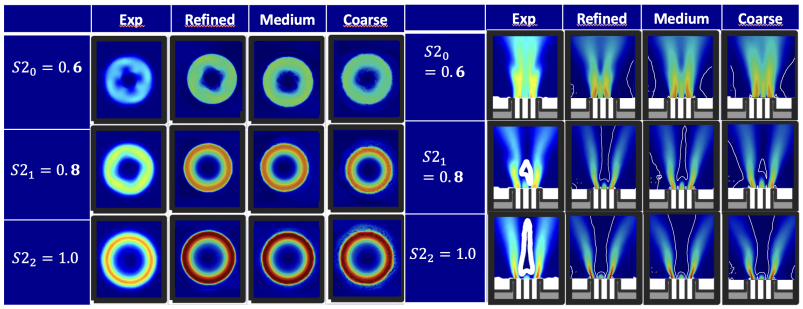

Fig. 3: Results for the non-reacting cases. On the left, the tangential velocity plots over the axial plane at 1.5mm from the injector lip. On the right, the axial velocity over a plane on the middle of the combustion chamber. In both results, the first column represents the experimental result next to the results obtained with the refined, medium, and coarse meshes in order..

3.2. Non-reacting cases of interest

The non-reacting cases of interest are characterized by $S_1 = 0$, meaning no metallic insert is used in the fuel channel, while the oxidizer swirl number S_2 is systematically varied. The study focuses on three specific values of S_2: 0.6, 0.8, and 1.0. The momentum flux ratio, defined in Eq. 3, is set at 4 to ensure consistent mass flow conditions across all cases.

A mesh refinement study was conducted for each selected condition using three levels of discretization. The initial coarse mesh consists of approximately 2.8 million tetrahedral cells, ensuring at least 10 grid points across the injection pipe walls, with a minimum mesh size of $\Delta x = 0.6$ mm. The first refinement step reduces Δx to 0.4 mm, increasing the total cell count to 9.3 million. A final refinement step, reducing Δx further to 0.2 mm, results in a highly resolved grid with 22 million cells.

Results from the mesh refinement study, presented in Fig. 3, indicate that while the coarse mesh captures the overall flow structures qualitatively, only the finest level of refinement fully resolves expected flow features. Specifically, the Central Recirculation Zone (CRZ), observed in the experimental setup, is not entirely captured in the coarser simulations. The tangential velocity plots highlight the impact of swirl number, where lower swirl values exhibit distinct patterns imprinted by the oxidizer slits, while higher swirl numbers lead to a more uniformly circular profile.

Discrepancies between numerical and experimental results are primarily attributed to physical boundary conditions rather than numerical discretization errors. A systematic offset of approximately 0.2 in swirl number can be noticed when comparing numerical results with experimental data, indicating an inlet boundary-induced deviation rather than a mesh resolution-related discrepancy.

4. Reacting Cases

Given the non-premixed burning condition of the OxyTec configuration and the complexity of methane combustion kinetics, tabulated chemistry was chosen as the most efficient approach for modelling combustion under these conditions. Specifically, the Flamelet Progress Variable (FPV) model was evaluated as an appropriate framework for adiabatic flame modelling, with the flexibility to extend into a non-adiabatic model such as the Radiative Flamelet Progress Variable (RFPV) model [11].

4.1. The Flamelet Progress Variable Model

To accurately capture the complex physics of oxy-combustion, the FPV model leverages tabulated chemistry to significantly reduce computational cost by limiting the number of transported scalars to three. This approach offers a substantial efficiency advantage over direct detailed chemistry simulations for complex schemes such as methane combustion.

The FPV framework is based on the generation of a flamelet library from counterflow non-premixed adiabatic flames subjected to varying strain rates. The first outcome of this process is the retrieval of an S-Curve for the fuel-oxidizer combination , methane air and subsequently, oxygen-enriched air. This curve can be further extended to include unstable branch of the S-Curve, thereby encompassing a broader range of combustion conditions, including lower-temperature flame states.

The flames within the database are remapped in terms of both mixture fraction (Z) and progress variable (Y_C). The selection of an appropriate progress variable is of paramount importance, as it must maintain the monotonicity of the tabulated quantities. Ensuring this property guarantees that each unique (Z, Y_C) pair corresponds to a single flamelet solution.

Once the flamelet library is constructed, it is further processed using a β-Probability Density Function (PDF) approach to incorporate a third dimension: the mixture fraction variance (Z''). This additional dimension accounts for subgrid-scale turbulence-chemistry interactions.

Finally, the tabulated chemistry model is integrated into the CFD solver, which subsequently solves for the transport equations governing the mixture fraction (Z), mixture fraction variance (Z''), and progress variable (C) as given in Eqs. 5, 6, and 7, respectively.

$$\frac{\partial \overline{\rho}\tilde{Z}}{\partial t} + \nabla \cdot (\overline{\rho}\tilde{u}\tilde{Z}) = \nabla \cdot [\overline{\rho}(\tilde{\alpha_Z} + \alpha_t)\nabla \tilde{Z}] \quad (5)$$

$$\frac{\partial \overline{\rho} \tilde{Z^{"}}^2}{\partial t} + \nabla \cdot (\overline{\rho} \tilde{u} \tilde{Z^{"}}^2) = \quad (6)$$
$$\nabla \cdot [\overline{\rho}(\alpha_{\tilde{Z^{"}}^2} + \alpha_t) \nabla \tilde{Z^{"}}^2] - \overline{\rho} \tilde{\chi}_{\tilde{Z}} + 2\overline{\rho}\alpha_t (\nabla \tilde{Z})^2$$
$$\frac{\partial \overline{\rho} \tilde{Y_C}}{\partial t} + \nabla \cdot (\overline{\rho} \tilde{u} \tilde{Y_C}) = \quad (7)$$
$$\nabla \cdot [\overline{\rho}(\alpha_{\tilde{Y_C}} + \alpha_t) \nabla \tilde{Y_C}] - \overline{\rho} \tilde{\omega}_{\tilde{Y_C}}$$

4.2. Radiative Flamelet Progress Variable Model

When analyzing combustion chambers in the context of oxy-combustion, two primary forms of heat loss must be considered: wall heat losses and radiative heat transfer.

In the tabulated chemistry approach, extending the framework to account for these losses is straightforward. From a tabulation perspective, an additional dimension must be incorporated to represent the enthalpy level of the flamelets. To achieve this, the 1D flame solver AGATH is employed. The procedure begins similarly to the FPV approach, where the stable branch of the S-Curve is retrieved. However, in this case, the unstable branch is not required. Instead, a prescribed heat loss is applied to the flamelets along the stable branch, followed by an unsteady simulation initiated from the adiabatic flame state. The simulation progresses until the imposed heat losses are fully integrated, leading to a new steady-state solution. The intermediate states are stored, enabling a proper mapping of the flamelet space to account for multiple enthalpy levels.

Heat losses are artificially introduced by scaling the radiative heat losses through an optically thin model [12]. This approach allows for controlled variation of the heat loss intensity by adding a scaling factor to the radiative power term. The optically thin model considers only emission losses while neglecting absorption, ensuring a straightforward implementation of heat losses through a radiative effects.

Following this procedure, a new parameter—the normalized enthalpy of the flamelet—is defined. In the adiabatic case, corresponding to the stable S-Curve branch, the enthalpy level is at its maximum since no losses occur. In contrast, all other solutions exhibit reduced enthalpy levels due to imposed losses. However, this method has a limitation: once the flame reaches a quenching point, its temperature decreases, leading to a reduction in heat losses and, consequently, an increase in the enthalpy level. This behavior marks the boundary of the RFPV model in its current implementation as the table would lose it's non monotonicity: it is not guaranteed that two different sets of coordinates ($\tilde{YC}$, $\tilde{Z}$, $\tilde{H}$) retrieve different flames. This factor limits the range of applicability of the RFPV model in its current implementation.

The CFD solver must also transport this additional enthalpy dimension as a passive scalar, Eq. 8.

$$\frac{\partial \overline{\rho} H}{\partial t} + \nabla \cdot (\overline{\rho} u H) = \nabla \cdot (\overline{\rho}(\alpha_H + \alpha_t) \nabla H) \quad (8)$$

Here, H represents the enthalpy scalar transported within the CFD software, effectively introducing a fourth transport equation to be solved in order to access the 4 dimensional flamelet table.

5. Results

The FPV model was initially applied in a validation case study to compare a one-dimensional (1D) flame solution obtained using the AGATH flame solver with a two-dimensional (2D) solution computed in YALES2 under an equivalent counterflow configuration. Once the YALES2 implementation was successfully validated, the model was then used to simulate Flame A0 from [1]. Finally, the limitations of the FPV model were assessed, leading to the development of the RFPV model as a strategy to address these constraints.

5.1. Combustion Model Validation

To evaluate the applicability of the FPV model within YALES2, a series of fundamental computations were performed. A 2D counterflow flame configuration was designed, in which fuel was injected from the top and oxidizer from the bottom. Two test cases were examined: one corresponding to a conventional methane-air combustion scenario and the other representing an oxygen-enriched methane combustion case, consistent with the OxyTec operating conditions. Both cases aimed to reproduce the flame structure at a strain rate of 400 $\frac{1}{s}$.

Figure 4 presents the temperature profiles of the two modelled flames. The boundary conditions were prescribed to enforce a stagnation plane at the centre of the domain, in accordance with a potential flow solution. This configuration ensures that the flame stabilizes in the lower half of the domain, where the oxidizer is introduced.

The oxygen-enriched case, shown on the left, exhibits a higher flame front temperature compared to the air-methane case. This behaviour aligns with expectations, as the increased oxygen concentration enhances the reactivity of the mixture, leading to a more intense combustion process.

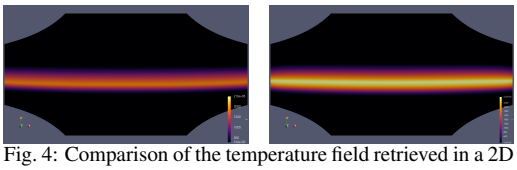

Fig. 4: Comparison of the temperature field retrieved in a 2D adiabatic counterflow case in YALES2. Air-methane (left) and Oxygen-enriched air-methane (right)

The one-dimensional (1D) flame generated in AGATH, which was used to tabulate values at the imposed strain rate, corresponds to the centerline of the computational domain shown in Fig. 4. Therefore, extracting key quantities along this line allows for a direct comparison between the tabulated flamelet data and the numerical results from YALES2.

For the methane-air case, the comparison shows an excellent match between the 1D flame solution and the 2D counterflow simulation. As illustrated in Figure 5, a slight discrepancy is observed in the velocity profile on the fuel side. However, this deviation is attributed to boundary effects rather than inconsistencies in the model. This conclusion is further supported by Figure 6, where the progress variable and density profiles show near-perfect agreement with the reference flamelet solution.

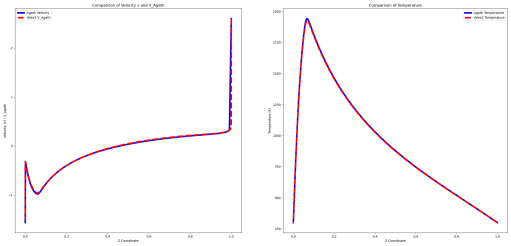

Fig. 5: Comparison of the velocity profile (left) and the temperature (right) over the mixture fraction

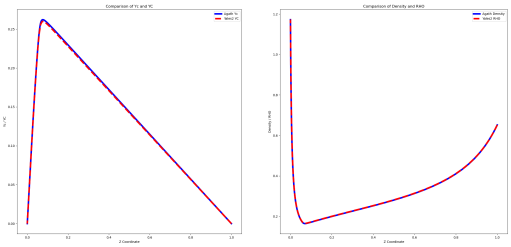

Fig. 6: Comparison of progress variable (left) and density (right) over the mixture fraction

When applying the same post-processing approach to the oxygen-enriched air case, the results also show strong agreement with the reference flamelet data. However, as illustrated in Figure 7, the discrepancies in the velocity profile are slightly more pronounced, particularly near the flame front, where a minor deviation is observed. Despite this, the overall consistency across all other variables, as shown in Figure 8, confirms that the observed differences are likely due to mesh effects rather than model inaccuracies.

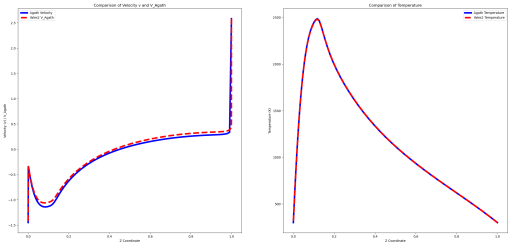

Fig. 7: Comparison of the velocity profile (left) and the temperature (right) over the mixture fraction

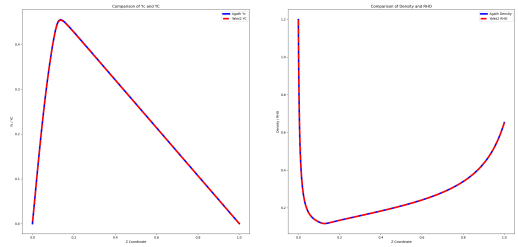

Fig. 8: Comparison of progress variable (left) and density (right) over the mixture fraction

5.2. Flame A0/A1 Results

The burning conditions of the Flame A0 and A1 are reported in Table 1. The only difference in between the two configurations is the metallic insert on the fuel line. From these inputs, retrieved from the experimental data, it is possible to define the mass flows of oxidizer and fuel. Combined with the definition of momentum flux ratio in Eq. 3 and the definition of the swirl number S2 in Eq. 2. The resulting mass flows are provided in Table 2.

The ratio between the tangential and axial oxidizer streams fixes the oxidizer swirl number S_2, while the flame properties set the ratio between fuel and oxidizer being injected.

The first result, related to the velocity field of the simulated flames, reported in Figure 9, outlines the robustness of the CFD solver in reproducing a complex swirled flow. The central recirculation zone (CRZ) is correctly recovered in both swirled conditions , particularly the closed geometry on the $S_1 = 0$ and it's evolution to an open CRZ at a higher swirl intensity.

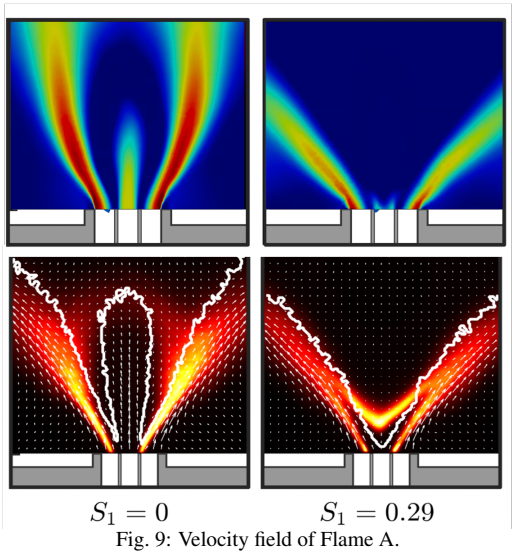

Fig. 9: Velocity field of Flame A.

To asses the refinement of the mesh, where a Δx =0.2mm is imposed in the flame region, the instantaneous fields of the OH field are plotted along the experimental result of a single snapshot in Figure 10.

Set	J	$\mathcal{P}_{th}$ [kW]	Φ	S_1	S_2	Re_2	$Y_{O_2,2}$	T_{ad} [K]	u_1 [m.s^{-1}]	u_2 [m.s^{-1}]
A-	4.0	9.4	0.40	0/0.29	0.85	12 000	0.40	1824	10.2	15.0

Table 1: Operating conditions for Flame A0 and A1.

Inlet	$S_2 = 0.85$
Fuel Stream	0.188 g/s
Axial Oxid. Stream	1.298 g/s
Tangential Oxid. Stream	3.464 g/s

Table 2: Inlet conditions and mass flow rates.

While there are some differences, particularly in the top par of the flame where the OH field is diffusing more in the flow, the pattern obtained in the numerical case is considered valid. Indeed, the adiabatic model being used is not well suited for oxy-combustion flames as the flame does not fully quenched in the higher region, but continuous burning resulting in a higher production of OH in the burnt gases.

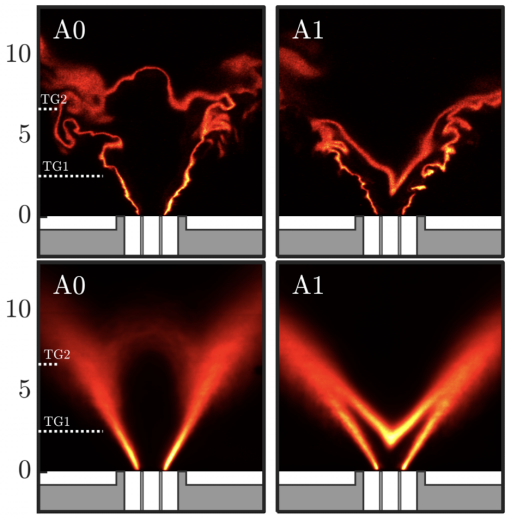

Fig. 10: Instantaneous field of Flame A.

In fact, when evaluating the averaged values of the OH field, an accumulation of the specie can be noticed in the higher part of the flame in Figure 11. In the higher part of the domain, where experimental results outline a quenched burnt gas region, a high concentration of OH is present. This indicates that, lacking heat losses such as radiation losses and heat transfer to the walls, the heat remains in the burnt gases, enabling reactions to continue until the upper region of the combustion chamber.

6. Conclusions

Declaration of competing interest

The authors declare that they have no known competing financial interests or personal relationships that could have appeared to influence the work reported in this paper.

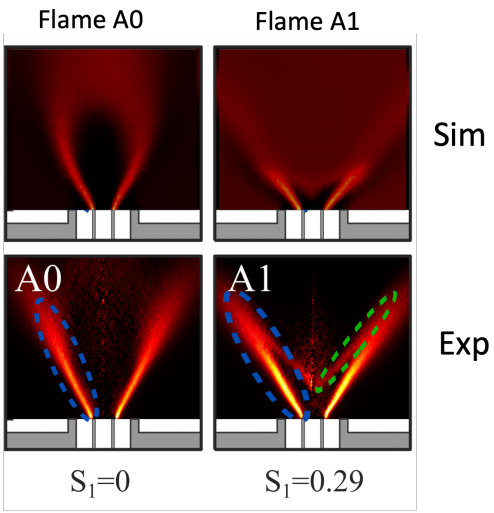

Fig. 11: Mean field of Flame A.

Acknowledgments

This study was conducted as part of the OXY3C project, funded by the French National Research Agency under the France 2030 program, ANR-22-PESP-0009.

References

[1] A. Degeneve, C. Mirat, J. Caudal, R. Vicquelin, T. Schuller, Effects of swirl on the stabilization of non-premixed oxygen-enriched flames above coaxial injectors, Journal of Engineering for Gas Turbines and Power 141 (12) (2019) 121018. doi:10.1115/1.4045024.

[2] S. Talei, D. Fozer, P. S. Varbanov, A. Szanyi, P. Mizsey, Oxyfuel combustion makes carbon capture more efficient, ACS Omega.

[3] M. A. Nemitallah, M. A. Habib, H. M. Badr, S. A. Said, A. Jamal, R. Ben-Mansour, E. M. A. Mokheimer, K. Mezghani, Oxy-fuel combustion technology: current status, applications, and trends, International Journal of Energy Research 41 (12) (2017) 1670–1708. doi:https://doi.org/10.1002/er.3722.

[4] M. Ihme, H. Pitsch, Modeling of radiation and nitric oxide formation in turbulent nonpremixed flames using a flamelet/progress variable formulation, Physics of Fluids 20 (5) (2008) 055110. doi:10.1063/1.2911047.

[5] V. Moureau, P. Domingo, L. Vervisch, Design of a massively parallel cfd code for complex geometries, Comptes Rendus Mécanique 339 (2)

(2011) 141–148, high Performance Computing. doi:https://doi.org/10.1016/j.crme.2010.12.001.
URL https://www.sciencedirect.com/science/article/pii/S1631072110002111

[6] H. Kishimoto, et al., Application of a nonadiabatic flamelet/progress-variable approach to les of h2o2 combustion under a pressurized condition, Fuel (2017). doi:10.1016/j.fuel.2017.11.127.

[7] Y.-S. Niu, L. Vervisch, P. Tao, An optimization-based approach to detailed chemistry tabulation: Automated progress variable definition, Combustion and Flame 160 (2013) 776–785. doi:10.1016/j.combustflame.2012.10.007.

[8] M. Bernard, G. Lartigue, G. Balarac, V. Moureau, G. Puigt, A framework to perform high-order deconvolution for finite-volume method on simplicial meshes, International Journal for Numerical Methods in Fluids 92 (11) (2020) 1551–1583. doi:https://doi.org/10.1002/fld.4839.

[9] J. H. Ferziger, M. Perić, R. L. Street, Computational methods for fluid dynamics, springer, 2019.

[10] M. Malandain, N. Maheu, V. Moureau, Optimization of the deflated conjugate gradient algorithm for the solving of elliptic equations on massively parallel machines, Journal of Computational Physics 238 (2013) 32–47. doi:https://doi.org/10.1016/j.jcp.2012.11.046.

[11] B. Fiorina, D. Veynante, S. Candel, Modeling combustion chemistry in large eddy simulation of turbulent flames, Flow, Turbulence and Combustion 94 (1) (2015) 3–42. doi:10.1007/s10494-014-9579-8.
URL https://hal.science/hal-01219272

[12] P. Rodrigues, Modélisation multiphysique de flammes turbulentes suitées avec la prise en compte des transferts radiatifs et des transferts de chaleur pariétaux.Thèse de doctorat dirigée par Darabiha, Nasser Combustion Université Paris-Saclay (ComUE) 2018 (2018).